Editors' Suggestion

Optical properties of vacancies in aluminum oxide (α-Al_2O_3) from first principles

Christoph Wilhelmer,[1,*] Mark E. Turiansky,[2,†] Dominic Waldhör,[1] Lukas Cvitkovich,[1,‡] Chris G. Van de Walle,[2] and Tibor Grasser[1,§]

[1]*Institute for Microelectronics, TU Wien, Gußhausstraße 27–29, 1040 Vienna, Austria*

[2]*Materials Department, University of California, Santa Barbara, California 93106-5050, USA*

(Received 16 June 2025; accepted 12 September 2025; published 30 September 2025)

We employ first-principles calculations based on hybrid density functional theory to investigate the structural and optical properties of the oxygen vacancy (V_O) and aluminum vacancy (V_{Al}) in α-Al_2O_3, the most stable (corundum) phase of alumina. Our calculations facilitate the identification of experimental excitation and luminescence spectra with specific electronic transitions at the vacancy sites. The absorption line shape for excitation of an electron at V_O^0 to the conduction-band minimum (CBM) is in excellent agreement with the 6.1 eV band detected by optical absorption spectroscopy, and we find that the 5.9 eV absorption band is generated by an internal electron transition at V_O^0. We confirm that the slowly decaying 3.0 eV emission band of the F center is due to a triplet-singlet transition at V_O^0. Our calculations also reveal that the 4.8 eV/5.4 eV absorption and 3.8 eV emission bands assigned to the F^+ center are generated by internal transitions at V_O^{+1}. The line shape for the excitation of an electron from V_O^{+1} to the CBM agrees well with an absorption band at 6.4 eV, while the recombination of an electron with V_O^{+2} also produces luminescence around 3.8 eV, but with a considerably broader line shape. For Al vacancies, we confirm that the most prevalent configuration in α-Al_2O_3 is a split-vacancy configuration $V_{Al,s}$, and we calculate migration barriers for different directions in the corundum crystal. We predict absorption and emission spectra for the excitation and recombination of an electron localized at V_{Al}^{-3} and $V_{Al,s}^{-3}$ sites with the CBM. The line shapes of the two V_{Al} configurations overlap and are considerably broader than the spectra corresponding to V_O.

DOI: 10.1103/5kvl-hktd

I. INTRODUCTION

Alumina (Al_2O_3) is a wide band-gap metal oxide with a broad range of applications in electronic devices. In metal-oxide-semiconductor (MOS) technologies, Al_2O_3 can be used as a high-κ gate dielectric [1], to passivate the surface of Si substrates [2] or as the tunneling layer of non-volatile flash memory devices [3]. Emerging devices with channels made of 2D materials frequently employ Al_2O_3 either as an insulator or as a buffer layer to HfO_2 [4,5]. Moreover, Al_2O_3 is frequently used in superconducting qubits. The key component in these devices is a Josephson junction, which is commonly realized as an Al/Al_2O_3/Al stack [6]. Al_2O_3 is also an attractive choice for the substrate of superconductor-based integrated circuits due to its exceptionally low dielectric loss value [7–9].

In all these devices, defects in the oxide layer can lead to reliability issues, as charges from the substrate can localize at the defect sites and consequently change the electrostatics. In MOS devices, this results in changes of important device characteristics such as the threshold voltage. Similarly, the quantum information of a qubit is sensitive to defect states [10] arising from defects in the substrate or in the tunnel barrier of the Josephson junction. Thus, to gain a better understanding of decoherence phenomena and to improve the performance of superconducting qubits and MOS devices, a thorough understanding of the structural, electronic, and optical properties of potential defect candidates is crucial.

Over the past decades, significant theoretical and experimental efforts have been devoted to analyzing the oxygen vacancy (V_O) in Al_2O_3 [11–36]. Removal of an oxygen atom from the corundum lattice results in two electrons remaining at the vacancy site in the neutral charge state. Removing one or both of these electrons results in V_O^{+1} or V_O^{+2} defects. The oxygen vacancy can be classified as a deep donor, as calculations [32] have shown it to have 0/+1 and +1/ + 2 charge-state transition levels (CTLs) deep inside the band gap.

In contrast, the aluminum vacancy (V_{Al}) can be classified as a deep acceptor since it can capture up to three additional electrons at the defect site [32,37]. Theoretical studies have predicted that the most stable configuration of the V_{Al} is a split vacancy ($V_{Al,s}$) [37–40]. In this configuration, an Al atom occupies the interstitial site halfway between two Al vacancies along the c-axis. To date, only the stable charge states and the

*Contact author: wilhelmer@iue.tuwien.ac.at

†Present Address: US Naval Research Laboratory, 4555 Overlook Avenue SW, Washington, DC 20375, USA.

‡Present Address: University of Regensburg, Universitätsstraße 31, D-93040 Regensburg, Germany.

§Contact author: grasser@iue.tuwien.ac.at

corresponding CTLs have been reported for vacancies in the corundum structure of alumina (α-Al_2O_3).

While the CTLs give a good estimate of the energetic position of optical transitions at the defect site, these levels alone can not account for the vibrational broadening as detected in spectroscopic measurements. The line shape of absorption and luminescence spectra gives information about the structural relaxations upon electronic transitions at the defect site. By considering optical transitions between vibronic levels of defects, it is possible to predict the form of the corresponding line shape and, therefore, to identify optical spectra with distinct electronic transitions at investigated defect sites [41].

This work aims to determine the optical and vibrational properties of vacancies in α-Al_2O_3 by means of first-principles calculations to guide the interpretation of spectroscopy measurements. According to the formation-energy analysis of Ref. [32], interstitials are less prevalent than vacancies. They also tend to have low migration barriers and are thus unlikely to occur as isolated defects. We therefore focus on vacancies in the present study. Following the approach by Alkauskas *et al.* [41], optical transitions at the vacancies are described with a configuration coordinate diagram (CCD), using parameters obtained from hybrid density functional theory (DFT) calculations. Structural relaxations upon charge trapping are characterized with an effective phonon mode. Based on these parameters, we calculate the absorption and emission line shapes for the neutral and positively charged oxygen vacancy.

First, we study the optical excitations of an electron localized at the vacancy site to the conduction-band minimum (CBM) and from the valence band to the vacancy. We also analyze internal transitions of an electron localized at V_O^0 and V_O^{+1} to higher unoccupied states localized at the vacancy site. This is followed by investigations of the recombination of an electron from the conduction band with a hole localized at the vacancy. In addition, we investigate the triplet-singlet transition at V_O^0. Our first-principles investigations are in good agreement with insights obtained from spectroscopic measurements [14,16–20,22–26]. We confirm the identification of the V_O^0 with the F center and of the V_O^{+1} with the F^+ center and provide details about different absorption and luminescence mechanisms that have not been considered so far.

We also investigate the optical and vibrational properties of the V_{Al}, including the energetically preferred split vacancy $V_{Al,s}$. To the best of our knowledge, the Al vacancy has not been identified with experimental optical spectra to date. Additionally, we calculate energy barriers for V_{Al} migration based on the climbing image nudged elastic band (CI-NEB) [42] and dimer [43] methods.

The paper is structured as follows: In Sec. II, the computational setup for the first-principles calculations is described. Details about the methodologies employed to determine the thermodynamic CTLs, to evaluate the strength of electron-phonon coupling, and to analyze the optical broadening of emission and absorption spectra are given. In Sec. III, the results of the calculations are presented and discussed. Energy barrier calculations for a transition from a V_{Al} to a $V_{Al,s}$ configuration in different charge states are presented. Absorption and luminescence line shapes for optical transitions at $V_{Al,s}$, V_{Al}, and V_O are calculated and compared to experimental spectroscopy measurements. Finally, in Sec. IV, we provide a short summary and conclusions.

II. METHODOLOGY

A. Computational setup

The DFT calculations were performed with the Gaussian plane wave (GPW) method as implemented in the CP2K code [44]. We employ the range-separated PBE0_TC_LRC hybrid functional [45] to accurately describe the electronic structure, in particular, the localization of charge at a defect site. The mixing parameter of this functional, which regulates the portion of the Hartree-Fock exchange, was set to 0.27, resulting in a band gap of 8.92 eV to match the experimental gap of corundum at room temperature (8.8-9.2 eV [30,46]). All calculations were carried out at the Γ point, and we employ a cutoff of 800 Ry for the expansion in the plane-wave basis set. To obtain a precise description of the vibrational modes of the defect structures, we enforce very tight convergence criteria for the energies and forces of 0.5 μeV and 0.8 meV $Å^{-1}$, respectively. Excited states were calculated within the non-Aufbau Δ self-consistent field (ΔSCF) approach [47], employing the maximum overlap method (MOM) [48] to force the occupation of a localized state above the CBM during the SCF cycle.

The cell parameters of the pristine bulk were relaxed until the residual stress was below 1 MPa, resulting in a mass density of 4.0 g cm^{-3}, which agrees with experimentally determined mass densities of corundum (3.984 g cm^{-3} [49]). The calculated lattice parameters of the 30-atom conventional cell of α-Al_2O_3 (space group $R\bar{3}c$) are $a = b = 4.76$ Å and $c = 12.97$ Å, which is in good agreement with the experimental values of $a = b = 4.76$ Å and $c = 12.99$ Å [50]. All Al atoms are bonded to 6 O atoms, while all O are bonded to 4 Al. Three of the six Al–O bonds have a bond length of 1.97 Å, the other three 1.86 Å. The bond lengths agree with experimental data from x-ray measurements (1.97 and 1.86 Å [50]).

All defect calculations were performed in a 240-atom supercell, which is obtained by taking a $4 \times 2 \times 1$ multiple of the 30-atom conventional cell and then converting it to an orthorhombic cell. The defect supercell containing a single vacancy was created by removing one atom and optimizing the geometry of the structure in different charge states. Migration paths between stable V_{Al} configurations were calculated with the CI-NEB method [42] and further optimized with the dimer method [43]. For the CI-NEB calculations, we use 16 intermediate images and a spring constant of 4.9 eV $Å^{-2}$. Convergence of the minimum energy path was achieved when the maximum force acting on the band was below 0.02 eV $Å^{-1}$ and the maximum displacement on the band was below 10^{-4} Å.

B. Charge-state transition level

The formation energy E^q_{form} of a defect in charge state q is given by [51]

$$E^q_{form} = E^q_{tot} - E^{bulk}_{tot} + \sum_i \mu_i n_i + qE_F + E^{corr}, \qquad (1)$$

where $E^q_{\rm tot}$ is the total energy of a supercell containing one defect in charge state q, and $E^{\rm bulk}_{\rm tot}$ is the total energy of the pristine bulk supercell. n_i is the number of atoms of type i removed from the system, and μ_i is the corresponding chemical potential. We referenced $\mu_{\rm O}$ to half of the energy of an O_2 molecule and $\mu_{\rm Al}$ to the energy of an Al atom in the aluminum crystal. The Fermi energy $E_{\rm F}$ is given with respect to the valence-band maximum (VBM) of the pristine bulk. $E^{\rm corr}$ is a correction term accounting for the spurious interactions of a charged supercell with its periodic image according to the Freysoldt-Neugebauer-Van de Walle correction scheme and the potential alignment of the bulk and defective supercell far away from the vacancy [52,53]. The correction term was calculated with a static dielectric tensor of $\varepsilon_{xx,yy,zz} = (8.63, 8.75, 10.6)$, as obtained from extracting the change of dipole moment according to the modern theory of polarization in a solid under a small applied constant electrical field [54,55].

The CTL corresponds to the Fermi energy, where the formation energies of two different charge states are equal and a transition in the lowest-energy charge state occurs. CTLs determine the electrical activity of a given defect and can be observed in electrical or optical measurements. The CTL (referenced to the VBM) is defined as

$$\varepsilon(q/q') = \frac{E^q_{\rm form}(E_{\rm F}=0) - E^{q'}_{\rm form}(E_{\rm F}=0)}{q'-q}, \qquad (2)$$

where the formation energies are evaluated at the VBM ($E_{\rm F} = 0$).

C. Electron-phonon coupling

When describing the dynamics of electron capture or release at a defect site, electron-phonon interactions have to be considered [41]. Upon localization of a charge carrier at a defect site, the attractive and repulsive forces change, and the system relaxes to a new minimum energy configuration. The strength of electron-phonon coupling for such a relaxation can be quantified by the Huang-Rhys factor S, which gives the average number of emitted phonons during structural relaxations upon charge trapping. A full description of this relaxation involves addressing a multidimensional vibrational problem. However, when S is sufficiently high ($S \gg 1$), such a transition can efficiently be described by a one-dimensional CCD diagram [56]. Such a diagram is shown for the $-3/-2$ transition of the $V_{\rm Al,s}$ in Fig. 1.

The effective mode of the transition is obtained by linearly interpolating images between the stable defect configurations. We then calculate the energies as a function of displacement in the two different charge states, corresponding to the ground and excited states [57–59]. The results of the energy calculations are depicted as circles. In the 1D harmonic approximation, the potential energy surface near the defect site is described by a parabolic function corresponding to the effective phonon mode $E(Q) = \frac{1}{2}\Omega^2 Q^2$. We explicitly verified that the harmonic approximation is well satisfied for all transitions studied here.

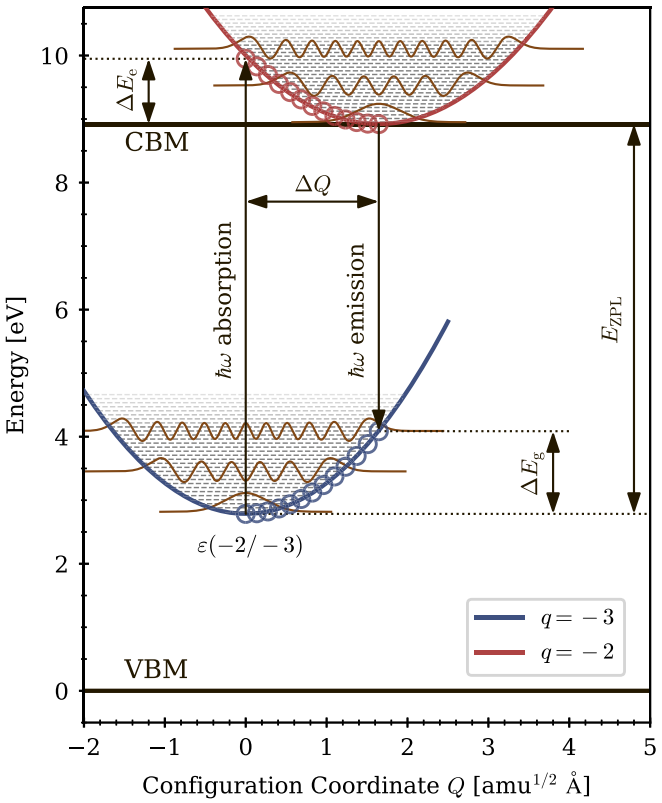

FIG. 1. 1D configuration coordinate diagram for the optical transitions between an electron localized at an aluminum split vacancy and the CBM. The $-2/-3$ CTL gives the energetic position of the defect state in the band gap. The potential energy curves in the ground (g) and excited (e) states are obtained by parabolic fits to the energies of linearly interpolated images between the two equilibrium configurations, which are depicted by the circles. $\Delta E_{\rm g,e}$ are the relaxation energies, $E_{\rm ZPL}$ represents the zero-phonon line, ΔQ the mass-weighted configuration coordinate change. The vibrational wave functions of the harmonic oscillators $\chi_{\rm g,e}$ are shown for $n, m = 0, 10, 20$.

Ω gives the frequency of the effective mode and

$$\Delta Q^2 = \sum_{\alpha,i} m_\alpha \Delta R^2_{\alpha i} \qquad (3)$$

gives the mass-weighted configuration coordinate change. Here, α is the index of the atom and $\Delta R_{\alpha i} = R_{{\rm e};\alpha i} - R_{{\rm g};\alpha i}$ the distortion vector with $R_{{\rm e};\alpha i}$ and $R_{{\rm g};\alpha i}$ being the coordinates i of the excited and ground state, respectively.

The position of the defect level in the band gap is determined by the CTL, with the energy difference between the equilibrium energies corresponding to the zero-phonon line $E_{\rm ZPL}$. Relaxation energies upon absorption or emission are denoted by $\Delta E_{\rm e,g}$ and are related to the Franck-Condon shift, the difference in energy between absorption and emission peaks. Within the 1D approximation, the Huang-Rhys factor of the optical transition is given by:

$$S_{\rm g,e} = \frac{\Delta E_{\rm g,e}}{\hbar\Omega_{\rm g,e}}, \qquad (4)$$

where $\Omega_{\rm g,e}$ are the vibrational frequencies of the ground (g) and excited (e) states.

D. Optical properties

Following the general theory of luminescence [60,61], the line shape function or normalized luminescence intensity of a dipole-allowed optical transition is given by

$$L_{\mathrm{em}}(\hbar\omega) = C\omega^3 A(\hbar\omega), \tag{5}$$

with $C^{-1} = \int A(\hbar\omega)\omega^3 d(\hbar\omega)$ and $A(\hbar\omega)$ being the spectral function

$$A(\hbar\omega) = \sum_{m,n} w_m(T)|\langle\chi_{em}|\chi_{gn}\rangle|^2 \cdot \delta(E_{\mathrm{ZPL}} + \hbar\Omega_{em} - \hbar\Omega_{gn} - \hbar\omega). \tag{6}$$

Here, $w_m(T)$ is the thermal occupation of the vibrational level m in the initial electronic state of the transition, which follows a Bose-Einstein distribution in thermal equilibrium. Optical transitions $m \to n$ are proportional to the so-called Franck-Condon overlap integrals $|\langle\chi_{em}|\chi_{gn}\rangle|$. The vibrational wave functions χ_n and χ_m are solutions of the quantum mechanical oscillator defined by the CCD. For calculations of the luminescence line shape functions, vibrational excitations ranging from 0 to $(m_{\max}, n_{\max}) = (20, 60)$ were considered. A Gaussian function with $\sigma = 0.6\hbar\Omega_{\mathrm{e}}$ was used to replace the Dirac delta function [41,56], which is the lowest value that allows obtaining a smooth line shape.

For $S \gg 1$, the temperature-dependent broadening of luminescence and absorption bands can reliably be predicted based on quantities derived from the 1D CCD [56]. Following [62], the full width at half maximum (FWHM) of the broadened emission spectrum as a function of the temperature T can be calculated with parameters extracted from the CCD:

$$W(T) = W_0\sqrt{\coth\left(\frac{\hbar\Omega_{\mathrm{e}}}{2k_{\mathrm{B}}T}\right)} = \sqrt{8\ln 2}\frac{S_{\mathrm{g}}\hbar\Omega_{\mathrm{g}}}{\sqrt{S_{\mathrm{e}}}}\sqrt{\coth\left(\frac{\hbar\Omega_{\mathrm{e}}}{2k_{\mathrm{B}}T}\right)}. \tag{7}$$

Starting from Eq. (6), the normalized absorption line shape can be expressed by [60,63]

$$L_{\mathrm{ab}}(\hbar\omega) = D\omega A(\hbar\omega) \tag{8}$$

with $D^{-1} = \int A(\hbar\omega)\omega d(\hbar\omega)$. The initial state prior to the transition is weighted by its thermal occupation $w_n(T)$, and vibrational excitations ranging from 0 to $(m_{\max}, n_{\max}) = (60, 20)$ are considered.

III. RESULTS AND DISCUSSION

A. Charge-state transition levels

An accurate calculation of the CTL is crucial for theoretically predicting the optical properties of defects. As can be seen in Fig. 1, the energy of the emitted or absorbed photon at the vacancy is related to the energetic position of the CTL relative to the band edges. Our results for CTLs are listed in Table I and compared with the previous results. While other details of the calculations, such as *a posteriori* corrections, also play a role, we attribute the differences mainly to the use of different functionals employed in the DFT calculations.

TABLE I. Calculated charge-state transition levels of vacancies in α-Al_2O_3. Results obtained with PBE0_TC_LRC are from this work; for comparison, results from previous work are listed, labeled with the functional used (in the case of LDA [37] and PBE [38,64] additional corrections were applied). All energy levels (in eV) are referenced to the VBM.

Defect $\varepsilon(q_1/q')$	PBE0	HSE [32]	PBE [38]/[64]	LDA [37]
V_{O} $\varepsilon(+2/+1)$	3.88	3.2	–/2.8	3.3
V_{O} $\varepsilon(+1/0)$	4.37	4.1	–/2.9	3.5
V_{Al} $\varepsilon(+4/+3)$	0.21			
V_{Al} $\varepsilon(+3/+2)$	0.57			
V_{Al} $\varepsilon(+2/+1)$	1.06			
V_{Al} $\varepsilon(+1/0)$	1.65			
V_{Al} $\varepsilon(0/-1)$	1.97	1.4	0.4/0.1	0.6
V_{Al} $\varepsilon(-1/-2)$	2.49	1.7	1.2/0.2	0.7
V_{Al} $\varepsilon(-2/-3)$	2.99	2.6	1.3/0.4	1.5
$V_{\mathrm{Al,s}}$ $\varepsilon(+4/+3)$	0.77			
$V_{\mathrm{Al,s}}$ $\varepsilon(+3/+1)$	0.84			
$V_{\mathrm{Al,s}}$ $\varepsilon(+1/0)$	1.54			
$V_{\mathrm{Al,s}}$ $\varepsilon(0/-1)$	1.85		0.4/–	0.3
$V_{\mathrm{Al,s}}$ $\varepsilon(-1/-2)$	2.26			0.7
$V_{\mathrm{Al,s}}$ $\varepsilon(-2/-3)$	2.53			1.0
Band gap	8.92	9.2	5.7/7.5	6.9

1. Oxygen vacancy

The results for the formation energy are shown in Fig. 2, and the corresponding CTLs are given in Table I.

For the V_{O}, $\varepsilon(0/+1)$ and $\varepsilon(+1/+2)$ are located near midgap and follow a $+2/+1/0$ progression with increasing Fermi energy. The lowest unoccupied molecular orbital (LUMO) of the V_{O} structure is delocalized, while the three next higher states are localized around the vacancy site in agreement with previous DFT results [29,65,66].

2. Aluminum vacancy

For both the V_{Al} and $V_{\mathrm{Al,s}}$, we find a large number of CTLs in the band gap, corresponding to varying occupations of the oxygen dangling-bond states surrounding the vacancy.

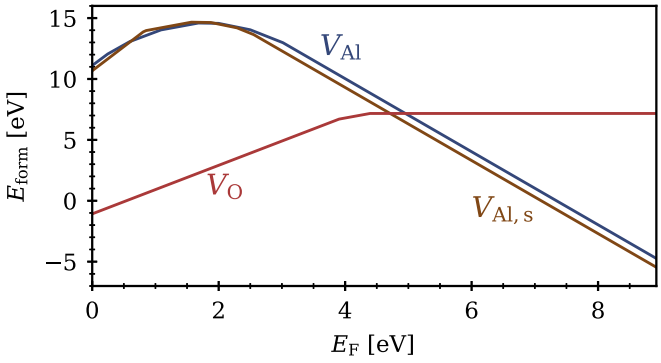

FIG. 2. Formation energy of the investigated vacancy configurations in α-Al_2O_3 as a function of the Fermi level. The related charge-state transition levels are given in Table I. The energy of V_{O} is shown for O-rich conditions, and the energy of V_{Al} for Al-rich conditions.

TABLE II. Migration barriers of V_{Al} in charge states $q = -3$ and $q = 0$, including results from Ref. [68] where indicated. The labeling of the Al positions is explained in Fig. 4.

Migration path	E_a for $q = 0$ [eV]	E_a for $q = -3$ [eV]
$V_{Al,4} \rightarrow V_{Al,int}$	1.93 [68]	1.71
$V_{Al,int} \rightarrow V_{Al,4}$	0.32 [68]	0.28
$V_{Al,int} \rightarrow V_{Al,3}$	0.32 [68]	0.24
$V_{Al,3} \rightarrow V_{Al,int}$	1.93 [68]	1.67
$V_{Al_1} \leftrightarrow V_{Al_2}$	1.80 [68]	1.59
$V_{Al_1} \leftrightarrow V_{Al_3}$	2.05 [68]	1.96
$V_{Al_2} \rightarrow V_{Al,s}$	1.97, 1.56 [68]	1.17
$V_{Al,s} \rightarrow V_{Al_4}$	1.92, 1.61 [68]	1.92

For Fermi energies above 2.99 eV (2.53 eV), V_{Al}^{-3} ($V_{Al,s}^{-3}$) is the most stable charge state. The formation energy of the V_{Al}^{0} configuration is 0.07 eV lower than for the $V_{Al,s}^{0}$. In contrast, the energy of V_{Al} is 0.02 eV higher for $q = -1$, 0.28 eV higher for $q = -2$ and 0.75 eV higher in energy for $q = -3$ compared to $V_{Al,s}$. These results qualitatively agree with the results of previous calculations, while quantitatively the calculated defect levels are considerably higher than with PBE [38,64] and LDA [37] due to the improved evaluation of the electronic band gap.

In addition to three unoccupied Kohn-Sham states within the band gap, the removal of an Al atom also introduces six occupied Kohn-Sham states in the lower part of the band gap, hybridized around the O atoms surrounding the vacancy. Adding electrons gives rise to the -1, -2, and -3 charge states, but positive charge states can also be generated by removing electrons; these positive charge states were not discussed in previous theoretical studies [32,37,38,64]. We find that up to four holes can be trapped, leading to the CTLs listed in Table I.

The atomic structure of V_{Al}^{-3} is shown in Fig. 3(a). As shown in Fig. 3(b) for $q = -3$, the $V_{Al,s}$ can be regarded as a complex consisting of an interstitial Al atom situated between two V_{Al} sites along the c-axis [37–40]. We verified that in α-Al_2O_3 the $V_{Al,s}$ is stable only in this orientation, unlike the case of β-Ga_2O_3, where due to the lower symmetry of the monoclinic structure, the split vacancy can occur in multiple orientations [67].

B. Aluminum vacancy migration

Migration barriers E_a for V_{Al}^{-3} were calculated with the dimer method. The migration paths are illustrated in Fig. 4, and the corresponding energy barriers for vacancy migration along these paths are given in Table II. For the V_{Al}^{-3} migration between the Al_3-Al_4 sites an intermediate metastable configuration $V_{Al,int}^{-3}$ was found which is 1.43 eV higher in energy than V_{Al}^{-3}. Results for these migration paths for V_{Al}^{0} were reported in Ref. [68]; we include these results in Table II. However, since the V_{Al}^{-3} and $V_{Al,s}^{-3}$ are stable for most Fermi levels within the band gap, the barriers for charge state $q = -3$ should govern the Al migration in α-Al_2O_3.

The path between $V_{Al_2}^{-3}$ [shown in Fig. 3(a)] and $V_{Al_4}^{-3}$ goes through the split-vacancy site $V_{Al,s}^{-3}$, which is lower in energy

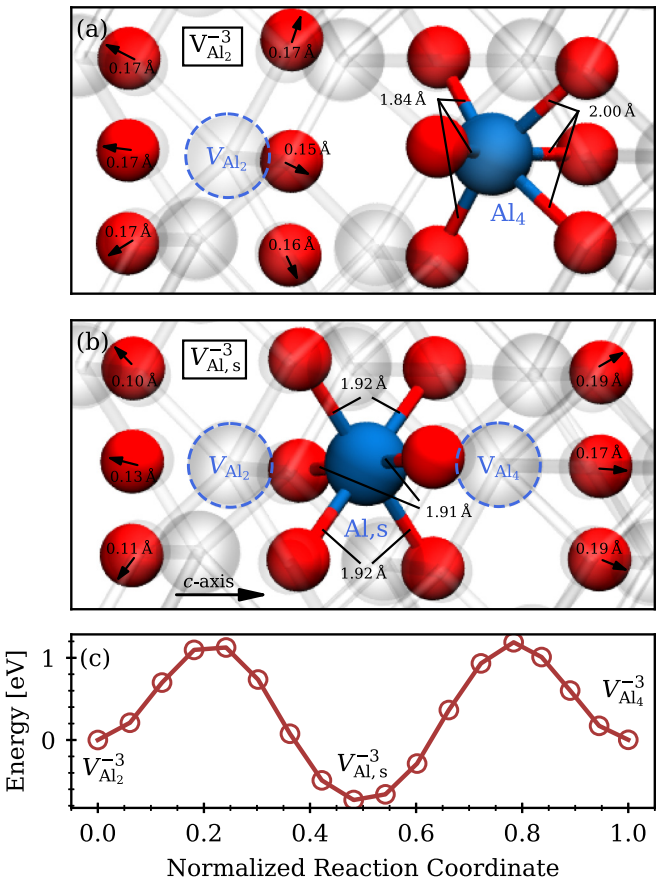

FIG. 3. (a) Rendering of α-Al_2O_3 with a V_{Al} defect relaxed in charge state $q = -3$. Al–O bond lengths are given, and the black arrows at O atoms show the direction and magnitude of relaxation referenced to positions in the perfect crystal. O atoms are drawn in red, Al in blue, Al vacancy positions are illustrated by a dashed circle. (b) Rendering of α-Al_2O_3 with a $V_{Al,s}$ defect relaxed in charge state $q = -3$. In this vacancy configuration, an Al atom occupies the interstitial site between two vacant Al sites along the c axis. (c) Migration barrier from V_{Al}^{-3} to $V_{Al,s}^{-3}$ to V_{Al}^{-3} as calculated with CI-NEB.

than those substitutional sites in the $q = -3$ charge state. We calculated this migration path between V_{Al} and $V_{Al,s}$ configuration with the CI-NEB method for $q = -3$ and $q = 0$. Slight asymmetries in the potential energy curve [Fig. 3(b)] are attributed to the image spacing of the CI-NEB method. The resulting barriers E_a are included in Table II for $q = 0$ and $q = -3$. The Al atom that moves toward the vacancy is originally at an adjacent lattice site along the c-axis. As this Al atom moves towards V_{Al}, it localizes at a new minimum-energy configuration corresponding to the $V_{Al,s}$ site. The energy barrier E_a therefore occurs for a position of the Al atom in between the V_{Al} and $V_{Al,s}$ configurations.

Our results confirm that the $V_{Al,s}$ is the prevalent cation deficiency configuration in α-Al_2O_3 [37–40]. The large energy difference $\Delta E = 0.75$ eV relative to V_{Al} for $q = -3$ indicates that most vacancies in the system occupy the split-vacancy state, since occupation ratios are given by the Boltzmann factor $e^{-(dE/k_BT)}$. Furthermore, once $V_{Al,s}$ forms, it is less likely to transition to V_{Al} compared to the reverse process due to the different energy barriers (see Table II).

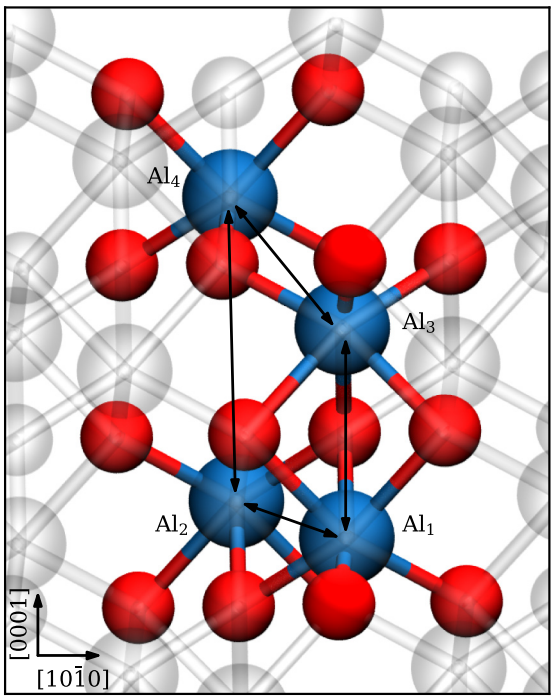

FIG. 4. Al positions for the calculated migration barriers of V_{Al} in the α-Al_2O_3 lattice viewed from the [1$\bar{2}$10] direction. O atoms are drawn in red and Al in blue. The [0001] direction corresponds to the c-axis of the crystal.

C. Optical properties

1. Configuration coordinate diagrams

We investigate optical transitions corresponding to the excitation of an electron from the vacancy site to the CBM and the corresponding recombination of an excited electron from the CBM with a hole localized at the vacancy site.

We also study the internal transitions of V_O^0 and V_O^{+1}, where the excited state ($V_O^{0^*}$) is evaluated with the ΔSCF method [47]. During the ΔSCF calculations, an electron at the vacancy site is promoted to a localized orbital above the CBM. During the structural relaxations, this occupied excited state shifts to below the CBM. The V_O^0 was also relaxed while enforcing a triplet electron configuration $V_O^{0^t}$. $V_O^{0^t}$ was further utilized to correct the multideterminant excited state of V_O^0 obtained from the ΔSCF approach to evaluate the energy of the excited singlet state [69]. We note that internal transitions were previously studied with time-dependent DFT, resulting in three internal absorption bands for both F and F^+ centers [27].

The effective parameters to model the potential energy curves in 1D upon charge trapping as described in Sec. II C were calculated for the $V_O^{0/+1}$, $V_O^{+1/+1^*}$, $V_O^{+1/+2}$, $V_O^{0/0^*}$, $V_O^{0/0^t}$, $V_{Al}^{-3/-2}$ and $V_{Al,s}^{-3/-2}$ transitions. The order in which the charge states are listed in the superscripts indicates initial/final states; e.g., for absorption $V_O^{0/+1}$ refers to the case where V_O^0 is the initial state and V_O^{+1} (plus an electron in the conduction band) the final state. For the V_O, the investigation of these specific transitions was motivated by the frequent identification of the F^+ and F centers with singly and doubly charged oxygen vacancies in experimental studies [22,26,30]. For both V_{Al} configurations, optical transitions from the vacancy in charge state $q = -3$ to the CBM were calculated. -3 is the most prevalent charge state of V_{Al} for a wide range of Fermi levels in the band gap (as discussed in Sec. III A 2).

For each investigated transition, 11 images were linearly interpolated between the atomic configurations of the equilibrium positions in the two different electron configurations. Effective frequencies $\Omega_{g,e}$ were obtained by fitting a parabolic function to the energies of the interpolated images as calculated with DFT. ΔQ was evaluated according to Eq. (3), S according to Eq. (4) and $W_0 = W(T = 0\ \mathrm{K})$ of the emission line shape according to Eq. (7). The resulting values are given in Table III. We note that the width of the absorption band of a certain transition can deviate from W_0 of the corresponding emission band due to different relaxation energies ($\Delta E_g \neq \Delta E_e$).

The removal of an electron from both the V_O^0 and the V_O^{+1} is accompanied by significant relaxations of the surrounding Al atoms away from the vacancy, resulting in the large ΔQ and Huang-Rhys factors of the $0/+1$ and $+1/+2$ transitions. For the Al vacancies, the atomic relaxations are not quite as large, but still result in significant ΔQ and S values.

2. Absorption

We first study optical absorption processes corresponding to the excitation of a localized electron at the vacancy site to the CBM. The line shapes of the absorption spectra for the $V_O^{0/+1}$, $V_O^{+1/+2}$, $V_{Al}^{-3/-2}$, and $V_{Al,s}^{-3/-2}$ transitions were calculated according to Eq. (8) with the effective parameters of the CCDs from Table III. We also calculate the absorption line shapes for the internal transitions of an electron at V_O^0 and V_O^{+1} to a higher unoccupied localized state at the vacancy. The results are shown in Fig. 5. Figure 5 also includes experimental spectra from Refs. [17,22–26]; the areas of all experimental spectra were normalized to 1 to facilitate comparison with calculated line shapes. To allow easier comparison with experimental data, the calculated spectra were slightly shifted; magnitudes of these shifts are given below. Such shifts could result from a variety of effects, such as slight inaccuracies in the charge correction schemes or typical DFT errors (e.g., self-interaction error) in the exchange-correlation functional [40,70–72]. The electronic defect levels and the calculated transitions assigned to absorption and luminescence bands of the F and F^+ center are summarized in Fig. 6.

For the $V_O^{0/+1}$ transition, our calculations reveal an absorption line shape centered in very good agreement with measurements for the F center [26], as shown in Fig. 5(a) (shift 0.13 eV). We thus assign the origin of the 6.1 eV absorption band to the V_O^0 defect, in agreement with insights obtained from experiments [16,22,23].

Experimentally, when the sample is kept in the dark for several weeks, only the 6.1 eV absorption band has been detected in nonoriented samples in Ref. [18] in the energy range between 3.0 and 6.5 eV. This strongly suggests that only F-centers (V_O^0 defects) were present in the equilibrated sample. Based on the calculated CTLs in Fig. 2 and Table I, we thus conclude that the Fermi level in these α-Al_2O_3 samples

TABLE III. Effective parameters of the optical transitions within the 1D approximation for vacancies in α-Al_2O_3. W_0 is the width of the emission lineshape at $T = 0$ K.

Defect$^{q_1/q_2}$	ΔQ [amu$^{1/2}$ Å]	$\hbar\Omega_g$ [meV]	$\hbar\Omega_e$ [meV]	S_g	S_e	E_{ZPL} [eV]	W_0 [eV]
$V_O^{0/0^*}$	2.75	26	29	23.6	25.7	5.42	0.29
$V_O^{0/0^t}$	2.91	27	30	26.9	29.9	3.35	0.31
$V_O^{0/+1}$	2.02	53	54	25.7	26.3	4.55	0.63
$V_O^{+1/+1^*}$	2.03	33	34	16.0	16.9	4.17	0.30
$V_O^{+1/+2}$	2.82	37	37	35.1	34.9	5.04	0.51
$V_{Al}^{-3/-2}$	1.58	67	60	20.0	17.2	5.92	0.76
$V_{Al,s}^{-3/-2}$	1.65	64	58	20.5	17.8	6.40	0.73

is above 4.3 eV. This also implies that all Al vacancies are in the $q = -3$ charge state.

The absorption band for the internal transition of the electron at the V_O^0 to the lowest unoccupied localized state at the vacancy site, giving rise to the $V_O^{0^*}$ excited state, is also shown in Fig. 5(a). It compares very well with the 5.9 eV absorption band detected by Weinstein *et al.* [24] (after applying a shift of −0.24 eV). Similar bands have also been reported in [23,34,35]. The 5.9 eV band observed in Ref. [35] exhibited the same annealing behavior as the 6.1 eV band, which is attributed to the $V_O^{0/+1}$ transition. As illustrated in Fig. 6, this strongly suggests that both bands have the same origin, namely V_O^0, in agreement with the assignments based on our calculations.

In Fig. 5(b), we show the absorption line shape for optical excitation of an electron localized at V_O^{+1} to the CBM; the calculated line shape is centered at 6.33 eV with a FWHM of 0.65 eV at $T = 293$ K. This compares very well with an absorption peak at 6.28 eV with an assigned FWHM of 0.68 ± 0.01 eV as detected in [24] (shift of −0.05 eV). A similar spectrum was tentatively related to an absorption band of the F^+ center in Ref. [17] with an assigned peak of 6.3 ± 0.2 eV and FWHM <0.8 eV. Furthermore, absorption peaks around 6.3 eV were detected in Refs. [25,26].

Figure 5(b) also shows the absorption band for the internal $V_O^{+1/+1^*}$ transition. This $V_O^{+1/+1^*}$ transition compares very well with the 4.8 eV absorption band assigned to the internal transition of the F^+ center from experimental literature [17,22] (after applying a shift of 0.12 eV). This absorption leads to luminescence with a peak at 3.8 eV as depicted

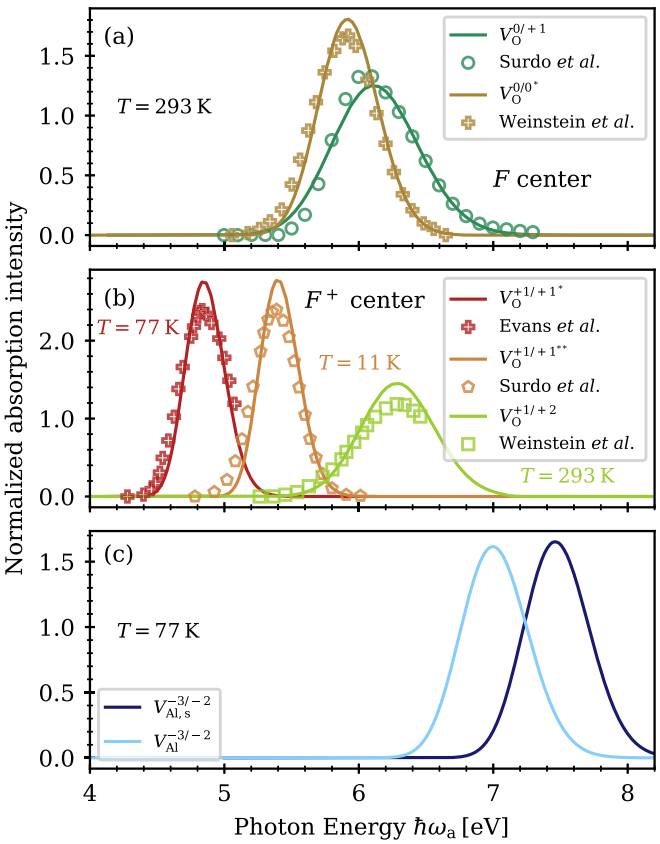

FIG. 5. (a) Absorption line shapes for the internal $V_O^{0/0^*}$ transition compared with spectroscopy data of the 5.9 eV excitation band (Weinstein *et al.* [25]) and the excitation of an electron from V_O^0 to the CBM compared with absorption spectroscopy data of the F center (Surdo *et al.* [26]). (b) Absorption line shapes for the internal $V_O^{+1/+1^*}$ and $V_O^{+1/+1^{**}}$ transitions and the excitation of an electron from V_O^{+1} to the CBM compared with measured absorption spectra assigned to the F^+ center (Evans *et al.* [17,22], Surdo *et al.* [23], Weinstein *et al.* [24]); (c) excitation of an electron from V_{Al}^{-3} or $V_{Al,s}^{-3}$ to the CBM. Calculated spectra were slightly shifted for better comparison with experimental data, as discussed in the text.

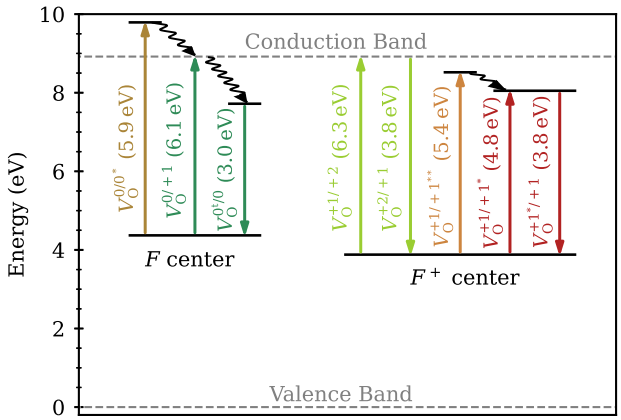

FIG. 6. Overview of optical transitions at the F and F^+ centers in α-Al_2O_3. Defect levels and transitions are drawn according to their E_{ZPL} and CTLs. The energies in parentheses next to the transitions indicate the peak energy of the respective band, which can be compared with experimental results. Wavy arrows denote nonradiative decay from excited states to lower energy states. The colors correspond to the respective lineshapes in Figs. 5 and 7.

in Fig. 6 and discussed in Sec. III C 3. Absorption bands at 4.8 eV were also detected in Refs. [12,15,17,18,25,28,34].

References [17,22,23] reported that absorption at ∼5.4 eV was also associated with emission at 3.8 eV. This absorption is distinct from the 4.8 eV peak, which we assigned to the internal $V_O^{+1/+1^*}$ transition above. The 5.4 eV absorption band was previously proposed to be generated by an internal transition to a higher localized state [14,22,27]. As shown in Fig. 6, our calculations indeed reveal the presence of a second localized state, with a Kohn-Sham state 0.47 eV higher in energy than the first localized state, very close to the difference in the peak energies of the 4.8 eV and 5.4 eV absorption bands.

Unfortunately, with our ΔSCF/MOM approach, we could not achieve stable occupation of this second localized state, which we label $V_O^{+1^{**}}$, and therefore could not explicitly calculate structural relaxations. As an approximation, we modeled the $V_O^{+1/+1^{**}}$ transition using the effective parameters of the $V_O^{+1/+1^*}$ transition, taking the difference in E_{ZPL} of the transitions as the energy difference between the two unoccupied Kohn-Sham states (0.47 eV). We indeed expect that the structural relaxations upon occupation of $V_O^{+1^{**}}$ would be comparable to those $V_O^{+1^*}$, since the wave functions of both states have a similar spatial distribution (hybridized over four Al around the vacancy) and both transitions preserve the charge state of the vacancy. The resulting absorption line shape for the $V_O^{+1/+1^{**}}$ transition compares well with the 5.4 eV excitation spectrum detected by Surdo *et al.* [23], as shown in Fig. 5(b) (after applying a shift of 0.20 eV).

The interpretations of our calculations also align with considerations concerning changes in defect density. In Ref. [35], it was demonstrated that the 4.8 eV, 5.4 eV, and the electron paramagnetic resonance (EPR) signal intensity of the F^+ center all exhibit the same annealing behavior over a large temperature range, suggesting that they have the same origin. Additionally, Ref. [18] showed that bleaching with 6.4 eV light increases both the 4.8 eV and 5.4 eV band when only F centers are present in the crystal. This increase is consistent with the generation of V_O^{+1} defects according to the $V_O^{0/+1}$ transition.

Absorption line shapes for band edge transitions of the aluminum vacancies are calculated for $T = 77$ K and shown in Fig. 5(c). The peaks of the line shapes are separated by 0.46 eV due to the different $\varepsilon(-2/-3)$ CTLs of the two distinct configurations. To the best of our knowledge, so far no absorption or excitation spectra above 6.5 eV have been related to specific defect centers. We note, however, that the Gaussian decomposition of the optical absorption spectrum in Ref. [34] suggests a broad peak at 7.6 eV that could correspond to the $V_{Al,s}^{-3/-2}$ transition.

3. Emission

We first calculate the emission line shapes according to Eq. (5) for the recombination of an electron from the CBM with a localized hole at the vacancy sites. The results for the $V_O^{+2/+1}$, $V_{Al}^{-2/-3}$ and $V_{Al,s}^{-2/-3}$ transitions are shown in Fig. 7(a). Additionally, Fig. 7(b) shows the triplet-singlet $V_O^{0^t/0}$ and internal $V_O^{+1^*/+1}$ transitions. The transitions at the oxygen vacancy and their assignments to experimental luminescence bands of the F and F^+ centers are summarized in the state diagram in Fig. 6. The temperature-dependent FWHM of the emission line shapes were calculated according to Eq. (7) and are shown in Fig. 7(c). Measurements of the FWHM as a function of T allow determining both the Huang-Rhys factor and the vibrational frequencies by fitting to Eq. (7).

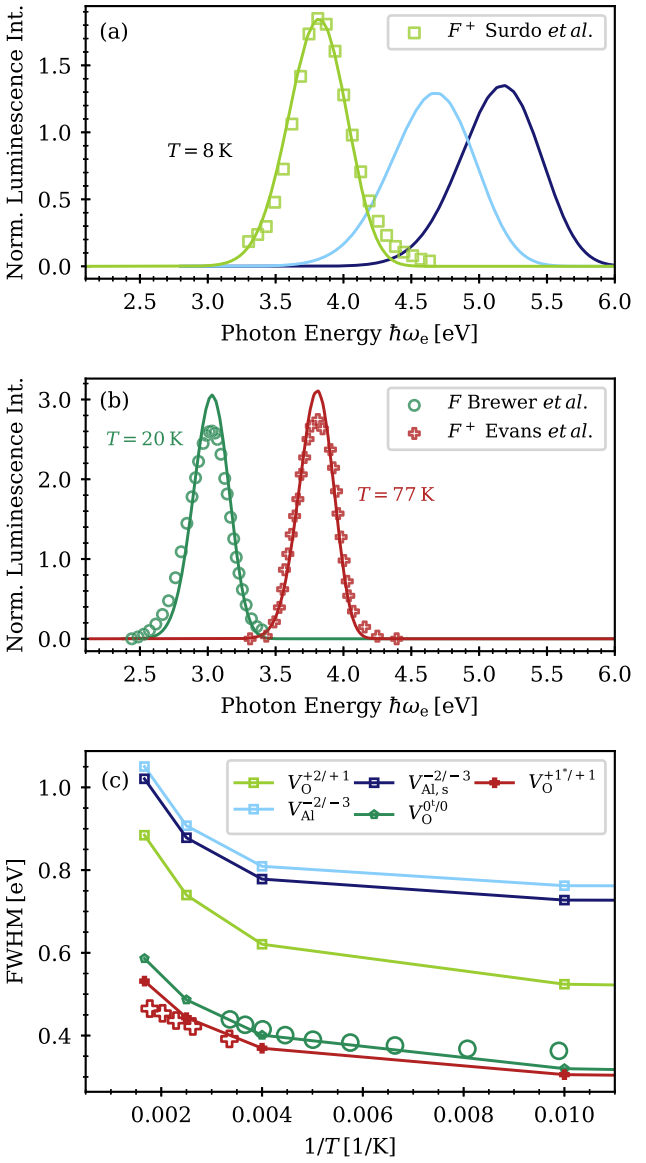

FIG. 7. (a) Calculated luminescence line shapes (solid lines) for the recombination of an electron at the CBM with a hole localized at V_O^{+2}, V_{Al}^{-2} or $V_{Al,s}^{-2}$ at $T = 8$ K. Colors correspond to the same transitions as given in the legend of panel (c). The data points denote the emission line shapes of the F^+ center as measured by Surdo *et al.* [26]. (b) Calculated luminescence line shapes (solid lines) for the triplet-singlet transition $V_O^{0^t/0}$ and the internal transition $V_O^{+1^*/+1}$. The data points denote emission line shapes of the F center as measured by Brewer *et al.* [19] and of the F^+ center as measured by Evans *et al.* [17,22]. Calculated spectra in (a) and (b) were slightly shifted to facilitate comparison with experimental data. The areas of the experimental spectra were normalized to 1. (c) FWHM of the calculated emission line shapes from (a) and (b) as a function of the temperature T in comparison with experimental data (same references as given in (b)). $W(T = 0\ \text{K})$ values are given in Table III.

For F^+, the line shape of $V_O^{+2/+1}$ for a transition from the CBM to V_O^{+2} in Fig. 7(a) is evaluated for $T = 8$ K to compare with experimental data from Ref. [26]. It was thereby shifted by +0.02 eV to match the experimental band centered at 3.8 eV. The line shape agrees well with the luminescence spectrum detected for the F^+ center [26] when the exciting light was polarized parallel to the c-axis of the crystal.

For the F center, we found that the $V_O^{0^*}$ state lies above the CBM and, consequently, E_{ZPL} of the $V_O^{0/0^*}$ transition is higher than the energy to ionize V_O^0 to V_O^{+1} [Fig. 5(a)]. We therefore believe that upon internal excitation, the electron at V_O^0 is rapidly lost to the conduction band (see Fig. 6), and luminescence according to a $V_O^{0^*/0}$ transition is unlikely to occur.

However, such a process would also effectively convert V_O^0 to V_O^{+1}. If the electron is captured by $V_O^{+1^*}$ and the vacancy subsequently relaxes to the ground state, it generates light according to an internal transition $V_O^{+1^*/+1}$ of the F^+ center. This might be the reason for the assignment of the 5.9 eV absorption band to the F^+ center in some experimental works [23,24]. Additionally, 5.9 eV light can excite an electron from V_O^{+1} to the CBM as shown in Fig. 5(b). When the electron at the CBM recombines with a hole at V_O^{+2}, it generates the broad luminescence band around 3.8 eV as shown in Fig. 7(a).

The luminescence band of the internal $V_O^{+1^*/+1}$ transition is shown in Fig. 7(b) for $T = 77$ K. The calculated line shape compares very well with the detected luminescence spectrum, with a peak at 3.8 eV assigned to internal transitions of the F^+ center from Refs. [17,22] (after applying a shift of +0.13 eV). Similar luminescence spectra were reported for the F^+ center in Refs. [18,30,33]. In these experimental studies, the 3.8 eV luminescence band was excited with light at either 4.8 eV or 5.4 eV, in agreement with absorption calculated for the internal $V_O^{+1/+1^*}$ and $V_O^{+1/+1^{**}}$ transitions in Sec. III C 2. For the 5.4 eV absorption, it is assumed that the V_O^{**} state quickly relaxes to V_O^*, which then gives the 3.8 eV emission [22] as illustrated in Fig. 6.

We obtain $W(0) = 0.30$ eV for the $V_O^{+1^*/+1}$ transition, which is close to the experimental value assigned to the F^+ center (0.34 eV [17] and 0.35 eV [18]). The temperature dependence of the broadening also agrees well with experimental data of the F^+ center luminescence [17] as shown in Fig. 7(c). Thus, we provide further evidence that the F^+ center in corundum is a V_O^{+1} defect and that the luminescence band at 3.8 eV is generated by the internal $V_O^{+1^*/+1}$ transition.

A luminescence band centered at 3.0 eV has also been attributed to the F center [18,19,26]; because of its long lifetime (in the millisecond range), it was suspected to originate from a triplet-singlet transition. Our calculated emission line shape for the triplet-singlet ($V_O^{0^t/0}$) transition is shown in Fig. 7(b). It is evaluated at $T = 20$ K to compare with a detected luminescence spectrum of the F center from Ref. [19] after applying a shift of +0.38 eV. The calculated broadening of $W(0) = 0.31$ eV is in reasonable agreement with the assigned experimental value of 0.36 eV [19]. Additionally, the detected temperature dependence of the FWHM [19] is well captured by our calculations, as shown in Fig. 7(c). Similar luminescence spectra centered at 3.0 eV were also related to the F center by other experimental works [22,26,30]. We note that direct recombination of an electron from the CBM with V_O^+1 would also result in emission with a peak around 3 eV, but with a much broader emission line shape ($W_0 = 0.63$ eV). Such a broad emission has not been detected by luminescence spectroscopy, to the best of our knowledge.

We propose the following mechanism for the formation of the triplet state: as discussed above and depicted in Fig. 6, excitation of an electron from V_O results in formation of V_O^{+1}, either by direct excitation to the conduction band, or by internal excitation followed by transfer of the electron to the conduction band. The electron can then get captured into the triplet state, $V_O^{0^t}$, by nonradiative decay. Our calculations thus confirm the assumption that the 3.0 eV luminescence band in α-Al_2O_3 is due to the triplet-singlet transition of the neutral oxygen vacancy.

The calculated emission line shapes for the $-2/-3$ transition at the aluminum vacancy are also included in Fig. 7(a), for both the V_{Al} and the $V_{Al,s}$ configurations. The spectra of V_{Al} and $V_{Al,s}$ overlap, with the peak of the split Al vacancy being 0.5 eV higher in energy compared to the single Al vacancy. To the best of our knowledge, no experimental papers have attempted to assign observed photoluminescence spectra to Al vacancies. Nevertheless, the positions of the calculated line shapes are in reasonable agreement with a broad luminescence band that was observed in Al_2O_3 between 200 and 350 nm (3.5 to 6.2 eV) [13] and was suggested to consist of multiple peaks. Peaks around 240 nm (5.2 eV) and 280 nm (4.4 eV) could be consistent with the line shapes shown in Fig. 7(a); the reported long lifetime is also consistent with the relatively low rate expected for electron capture onto a -2 charge state.

In Fig. 7(c), we also show the calculated FWHM of the spectra as a function of temperature. The width of the $V_{Al}^{-2/-3}$ emission spectrum is slightly larger compared to the width of the $V_{Al,s}^{-2/-3}$ transition due to the larger effective frequencies.

IV. SUMMARY AND CONCLUSION

We have characterized vacancies in α-Al_2O_3 with hybrid functional calculations in the supercell approach and evaluated optical emission and absorption processes at the defect sites with a configuration coordinate model. Our formation energy and CI-NEB calculations indicate that the Al vacancy (V_{Al}) is likely to form in a split-vacancy configuration $V_{Al,s}$, where an Al atom occupies an interstitial position between two V_{Al} sites in the corundum lattice along the c-axis. Migration barriers for V_{Al}^{-3} were evaluated with the dimer method for different directions in the corundum crystal.

We also calculated absorption and emission line shapes for the exchange of carriers between the vacancies and the band edges, as well as for internal transitions. The results are summarized in Fig. 6.

The calculated absorption line shape of the $V_O^{0/+1}$ transition closely matches spectroscopic measurements for the F center centered around 6.1 eV. In agreement with experimental assumptions, our calculations demonstrate that the 3.0 eV luminescence band of the F center is due to an internal triplet-singlet transition at V_O^0. Additionally, we argue that the 5.9 eV

absorption band is generated by an internal transition of an electron at V_O^0 to a localized state above the CBM. When the excited electron relaxes to the CBM or to an excited state of the F^+ center, it can generate light at 3.8 eV in agreement with suggestions in experimental papers.

The calculated absorption and emission line shapes of the V_O^{+1} closely match spectroscopy data assigned to the F^+ center. We find that the 4.8 eV and 5.4 eV absorption bands are related to internal transitions of the localized electron at V_O^{+1}. These transitions also produce the characteristic F^+ center emission band at 3.8 eV.

Additionally, we find the absorption band for excitation of an electron at V_O^{+1} to the CBM to be in reasonable agreement with absorption spectroscopy data centered around 6.4 eV. The calculated luminescence line shape for a transition of an electron from the CBM to V_O^{+2} is in excellent agreement with the observed broader emission spectrum of the F^+ center, which overlaps with the internal transition centered at 3.8 eV. Our first-principles calculations thus give evidence for the identification of the F^+ center with the singly charged oxygen vacancy.

We also report calculated absorption and luminescence spectra for the exchange of an electron at V_{Al}^{-3} and $V_{Al,s}^{-3}$ with the CBM. The line shapes of both Al vacancy configurations are broader than for the V_O, and they overlap with a peak separation of 0.5 eV. We hope that these predictions will aid in the identification of the microscopic origin of experimentally observed lines.

ACKNOWLEDGMENTS

C.W. and D.W. thank A. Shluger and J. Strand for helpful discussions. C.W., D.W., L.C., and T.G. were supported by the European Union's Horizon 1.1 – European Research Council (ERC) program under Grant Agreement No. 101055379, within the framework of the project Fluorides for 2D Next-Generation Nanoelectronics (F2GO). M.E.T. was supported by the U.S. Department of Energy, Office of Science, National Quantum Information Science Research Centers, Co-design Center for Quantum Advantage (C2QA) under Contract No. DE-SC0012704. Additional support was provided by a Vannevar Bush Faculty Fellowship from the Office of Naval Research (N00014-22-1-2808). This work used Expanse at SDSC through Allocation No. DMR070069 from the Advanced Cyberinfrastructure Coordination Ecosystem: Services & Support (ACCESS) program, which is supported by U.S. National Science Foundation Grants No. 2138259, No. 2138286, No. 2138307, No. 2137603, and No. 2138296. The computational results have been achieved using the Austrian Scientific Computing (ASC) infrastructure. The authors acknowledge TU Wien Bibliothek for financial support through its Open Access Funding Programme.

DATA AVAILABILITY

The data that support the findings of this article are not publicly available. The data are available from the authors upon reasonable request.

[1] S. Huang, X. Wang, Y. Yao, K. Deng, Y. Yang, Q. Jiang, X. Liu, F. Guo, B. Shen, K. J. Chen, and Y. Hao, Threshold voltage instability in III-nitride heterostructure metal–insulator–semiconductor high-electron-mobility transistors: Characterization and interface engineering, Appl. Phys. Rev. **11**, 021325 (2024).

[2] S. Banerjee and M. K. Das, A review of Al_2O_3 as surface passivation material with relevant process technologies on c-Si solar cell, Opt. Quantum Electron. **53**, 60 (2021).

[3] D. Kim, C.-M. Song, S. J. Heo, G. Pyo, D. Kim, J. H. Lee, K.-H. Park, S. Lee, H.-J. Kwon, and J. E. Jang, Nonvolatile flash memory device with ferroelectric blocking layer via *in situ* ALD process, Appl. Phys. Lett. **123**, 042904 (2023).

[4] P. Zhao, A. Padovani, P. Bolshakov, A. Khosravi, L. Larcher, P. K. Hurley, C. L. Hinkle, R. M. Wallace, and C. D. Young, Understanding the impact of annealing on interface and border traps in the $Cr/HfO_2/Al_2O_3/MoS_2$ system, ACS Appl. Electron. Mater. **1**, 1372 (2019).

[5] D. Zeng, Z. Zhang, Z. Xue, M. Zhang, P. K. Chu, Y. Mei, Z. Tian, and Z. Di, Single-crystalline metal-oxide dielectrics for top-gate 2D transistors, Nature (London) **632**, 788 (2024).

[6] L. Zeng, D. Tran, C.-W. Tai, G. Svensson, and E. Olsson, Atomic structure and oxygen deficiency of the ultrathin aluminium oxide barrier in $Al/AlO_x/Al$ Josephson junctions, Sci. Rep. **6**, 29679 (2016).

[7] E. K. Hollmann, O. G. Vendik, A. G. Zaitsev, and B. T. Melekh, Substrates for high-T_c superconductor microwave integrated circuits, Supercond. Sci. Technol. **7**, 609 (1994).

[8] K. M. Law, S. Budhathoki, S. Ranjit, F. Martin, A. S. Thind, R. Mishra, and A. J. Hauser, Demonstration of nearly pinhole-free epitaxial aluminum thin films by sputter beam epitaxy, Sci. Rep. **10** (2020).

[9] M. E. Turiansky and C. G. Van de Walle, Dielectric loss due to charged-defect acoustic phonon emission, APL Quantum **1**, 026114 (2024).

[10] L. Tian and R. W. Simmonds, Josephson junction microscope for low-frequency fluctuators, Phys. Rev. Lett. **99**, 137002 (2007).

[11] E. W. J. Mitchell, J. D. Rigden, and P. D. Townsend, The anisotropy of optical absorption induced in sapphire by neutron and electron irradiation, Philos. Mag. **5**, 1013 (1960).

[12] P. W. Levy, Color centers and radiation-induced defects in Al_2O_3, Phys. Rev. **123**, 1226 (1961).

[13] W. A. Runciman, Sapphire luminescence under X-ray excitation, Solid State Commun. **6**, 537 (1968).

[14] S. Y. La, R. H. Bartram, and R. T. Cox, The F^+ center in reactor-irradiated aluminum oxide, J. Phys. Chem. Solids **34**, 1079 (1973).

[15] T. J. Turner and J. H. Crawford, Jr., Nature of the 6.1-eV band in neutron-irradiated Al_2O_3 single crystals, Phys. Rev. B **13**, 1735 (1976).

[16] K. H. Lee and J. H. Crawford, Jr., Electron centers in single-crystal Al_2O_3, Phys. Rev. B **15**, 4065 (1977).

[17] B. D. Evans and M. Stapelbroek, Optical properties of the F^+ center in crystalline Al_2O_3, Phys. Rev. B **18**, 7089 (1978).

[18] B. G. Draeger and G. P. Summers, Defects in unirradiated α-Al_2O_3, Phys. Rev. B **19**, 1172 (1979).

[19] J. D. Brewer, B. T. Jeffries, and G. P. Summers, Low-temperature fluorescence in sapphire, Phys. Rev. B **22**, 4900 (1980).

[20] S.-i. Choi and T. Takeuchi, Electronic states of F-type centers in oxide crystals: A new picture, Phys. Rev. Lett. **50**, 1474 (1983).

[21] B. D. Evans, G. J. Pogatshnik, and Y. Chen, Optical properties of lattice defects in α-Al_2O_3, Nucl. Instrum. Methods Phys. Res. **91**, 258 (1994).

[22] B. D. Evans, A review of the optical properties of anion lattice vacancies, and electrical conduction in α-Al_2O_3: their relation to radiation-induced electrical degradation, J. Nucl. Mater. **219**, 202 (1995).

[23] A. I. Surdo, V. S. Kortov, and V. A. Pustovarov, Luminescence of F and F^+ centers in corundum upon excitation in the interval from 4 to 40 eV, Radiat. Meas. **33**, 587 (2001).

[24] I. A. Weinstein and V. S. Kortov, The shape and the temperature dependence of the main band in UV absorption spectra of TLD-500 dosimetric crystals, Radiat. Meas. **33**, 763 (2001).

[25] I. A. Weinstein, V. E. Pelenyov, and V. S. Kortov, The effect of thermally stimulated photoconversion of oxygen centres on the sensitivity of TLD-500 dosimetric crystals, Radiat. Prot. Dosim. **100**, 159 (2002).

[26] A. I. Surdo, V. S. Kortov, V. A. Pustovarov, and V. Y. Yakovlev, UV luminescence of F-centers in aluminum oxide, Phys. Status Solidi C **2**, 527 (2005).

[27] J. Carrasco, N. Lopez, C. Sousa, and F. Illas, First-principles study of the optical transitions of F centers in the bulk and on the (0001) surface of α-Al_2O_3, Phys. Rev. B **72**, 054109 (2005).

[28] M. Itou, A. Fujiwara, and T. Uchino, Reversible photoinduced interconversion of color centers in α-Al_2O_3 prepared under vacuum, J. Phys. Chem. C **113**, 20949 (2009).

[29] V. A. Pustovarov, V. S. Aliev, T. V. Perevalov, V. A. Gritsenko, and A. P. Eliseev, Electronic structure of an oxygen vacancy in Al_2O_3 from the results of ab initio quantum-chemical calculations and photoluminescence experiments, J. Exp. Theor. Phys. **111**, 989 (2010).

[30] Y. Zorenko, T. Zorenko, T. Voznyak, A. Mandowski, Q. Xia, M. Batentschuk, and J. Friedrich, Luminescence of F^+ and F centers in Al_2O_3-Y_2O_3 oxide compounds, IOP Conf. Ser. Mater. Sci. Eng. **15**, 012060 (2010).

[31] M. Izerrouken and T. Benyahia, Absorption and photoluminescence study of Al_2O_3 single crystal irradiated with fast neutrons, Nucl. Instrum. Methods Phys. Res., Sect. B **268**, 2987 (2010).

[32] M. Choi, A. Janotti, and C. G. Van de Walle, Native point defects and dangling bonds in α-Al_2O_3, J. Appl. Phys. **113**, 044501 (2013).

[33] D. V. Ananchenko, S. V. Nikiforov, G. R. Ramazanova, R. I. Batalov, R. M. Bayazitov, and H. A. Novikov, Luminescence of F-type defects and their thermal stability in sapphire irradiated by pulsed ion beams, Opt. Spectrosc. **128**, 207 (2020).

[34] A. Lushchik, V. N. Kuzovkov, E. A. Kotomin, G. Prieditis, V. Seeman, E. Shablonin, E. Vasil'chenko, and A. I. Popov, Evidence for the formation of two types of oxygen interstitials in neutron-irradiated α-Al_2O_3 single crystals, Sci. Rep. **11**, 20909 (2021).

[35] A. Lushchik, V. N. Kuzovkov, I. Kudryavtseva, A. I. Popov, V. Seeman, E. Shablonin, E. Vasil'chenko, and E. A. Kotomin, The two types of oxygen interstitials in neutron-irradiated corundum single crystals: Joint experimental and theoretical study, Phys. Status Solidi B **259**, 2100317 (2022).

[36] T. Cavignac, M. Vigier, E. Fritsch, P. Deniard, S. Jobic, and C. Latouche, Luminescence properties of Al_2O_3: Ti in the blue and red regions: A combined theoretical and experimental study, Inorg. Chem. **63**, 2934 (2024).

[37] N. D. M. Hine, K. Frensch, W. M. C. Foulkes, and M. W. Finnis, Supercell size scaling of density functional theory formation energies of charged defects, Phys. Rev. B **79**, 024112 (2009).

[38] A. Sundar and L. Qi, Stability of native point defects in α-Al_2O_3 under aqueous electrochemical conditions, J. Appl. Electrochem. **51**, 639 (2021).

[39] A. Venzie, A. Portoff, M. Stavola, W. B. Fowler, J. Kim, D.-W. Jeon, J.-H. Park, and S. J. Pearton, H trapping at the metastable cation vacancy in α-Ga_2O_3 and α-Al_2O_3, Appl. Phys. Lett. **120**, 192101 (2022).

[40] A. Kononov, C.-W. Lee, E. P. Shapera, and A. Schleife, Identifying native point defect configurations in α-alumina, J. Phys.: Condens. Matter **35**, 334002 (2023).

[41] A. Alkauskas, J. L. Lyons, D. Steiauf, and C. G. Van de Walle, First principles calculations of luminescence spectrum line shapes for defects in semiconductors: The example of GaN and ZnO, Phys. Rev. Lett. **109**, 267401 (2012).

[42] G. Henkelman, B. P. Uberuaga, and H. Jónsson, A climbing image nudged elastic band method for finding saddle points and minimum energy paths, J. Chem. Phys. **113**, 9901 (2000).

[43] G. Henkelman and H. Jónsson, A dimer method for finding saddle points on high-dimensional potential surfaces using only first derivatives, J. Chem. Phys. **111**, 7010 (1999).

[44] T. D. Kühne, M. Iannuzzi, M. Del Ben, V. V. Rybkin, P. Seewald, F. Stein *et al.*, CP2K: An electronic structure and molecular dynamics software package - Quickstep: Efficient and accurate electronic structure calculations, J. Chem. Phys. **152**, 194103 (2020).

[45] M. Guidon, J. Hutter, and J. VandeVondele, Robust periodic Hartree-Fock exchange for large-scale simulations using Gaussian basis sets, J. Chem. Theory Comput. **5**, 3010 (2009).

[46] R. H. French, Electronic band structure of Al_2O_3, with comparison to AlON and AlN, J. Am. Ceram. Soc. **73**, 477 (1990).

[47] J. Gavnholt, T. Olsen, M. Engelund, and J. Schiøtz, Δ self-consistent field method to obtain potential energy surfaces of excited molecules on surfaces, Phys. Rev. B **78**, 075441 (2008).

[48] G. M. J. Barca, A. T. B. Gilbert, and P. M. W. Gill, Simple models for difficult electronic excitations, J. Chem. Theory Comput. **14**, 1501 (2018).

[49] R. W. G. Wyckoff, *Crystal Structures*, 2nd ed., Vol. 2. (Sydney Interscience Publishers, New York, London, 1964).

[50] R. R. Newnham and Y. M. de Haan, Refinement of the αAl_2O_3, Ti_2O_3, V_2O_3 and Cr_2O_3 structures, Z. Kristallogr. **117**, 235 (1962).

[51] C. Freysoldt, B. Grabowski, T. Hickel, J. Neugebauer, G. Kresse, A. Janotti, and C. G. Van de Walle, First-principles calculations for point defects in solids, Rev. Mod. Phys. **86**, 253 (2014).

[52] C. Freysoldt, J. Neugebauer, and C. G. Van de Walle, Fully *ab initio* finite-size corrections for charged-defect supercell calculations, Phys. Rev. Lett. **102**, 016402 (2009).

[53] C. Freysoldt, J. Neugebauer, and C. G. Van de Walle, Electrostatic interactions between charged defects in supercells, Phys. Status Solidi B **248**, 1067 (2011).

[54] N. A. Spaldin, A beginner's guide to the modern theory of polarization, J. Solid State Chem. **195**, 2 (2012).

[55] M. Stengel, N. A. Spaldin, and D. Vanderbilt, Electric displacement as the fundamental variable in electronic-structure calculations, Nat. Phys. **5**, 304 (2009).

[56] A. Alkauskas, M. D. McCluskey, and C. G. Van de Walle, Tutorial: Defects in semiconductors—Combining experiment and theory, J. Appl. Phys. **119**, 181101 (2016).

[57] A. M. Stoneham, *Theory of Defects in Solids* (Clarendon Press, Oxford, 1975).

[58] A. M. Stoneham and R. H. Bartram, Non-radiative de-excitation of deep centres, Solid-State Electron. **21**, 1325 (1978).

[59] A. Alkauskas, Q. Yan, and C. G. Van de Walle, First principles theory of nonradiative carrier capture via multiphonon emission, Phys. Rev. B **90**, 075202 (2014).

[60] M. Lax, The Franck-Condon principle and its application to crystals, J. Chem. Phys. **20**, 1752 (1952).

[61] K. Huang and A. F. Rhys, Theory of light absorption and non-radiative transitions in F-centres, Proc. R. Soc. A **204**, 406 (1950).

[62] M. A. Reshchikov and H. Morkoç, Luminescence properties of defects in GaN, J. Appl. Phys. **97**, 061301 (2005).

[63] J. J. Markham, Interaction of normal modes with electron traps, Rev. Mod. Phys. **31**, 956 (1959).

[64] T. Watcharatharapong, J. T-Thienprasert, and S. Limpijumnong, Theoretical study of optical properties of native point defects in α-Al_2O_3, Integr. Ferroelectr. **156**, 79 (2014).

[65] D. Liu and J. Robertson, Oxygen vacancy levels and interfaces of Al_2O_3, Microelectron. Eng. **86**, 1668 (2009).

[66] O. A. Dicks, J. Cottom, A. L. Shluger, and V. V. Afanas'ev, The origin of negative charging in amorphous Al_2O_3 films: the role of native defects, Nanotechnology **30**, 205201 (2019).

[67] Y. K. Frodason, J. B. Varley, K. M. H. Johansen, L. Vines, and C. G. Van de Walle, Migration of Ga vacancies and interstitials in β–Ga_2O_3, Phys. Rev. B **107**, 024109 (2023).

[68] Y. Lei, Y. Gong, Z. Duan, and G. Wang, Density functional calculation of activation energies for lattice and grain boundary diffusion in alumina, Phys. Rev. B **87**, 214105 (2013).

[69] U. von Barth, Local-density theory of multiplet structure, Phys. Rev. A **20**, 1693 (1979).

[70] J. L. Bao, L. Gagliardi, and D. G. Truhlar, Self-interaction error in density functional theory: An appraisal, J. Phys. Chem. Lett. **9**, 2353 (2018).

[71] H.-P. Komsa, T. Rantala, and A. Pasquarello, Comparison between various finite-size supercell correction schemes for charged defect calculations, Phys. B: Condens. Matter **407**, 3063 (2012).

[72] P. Deák, M. Lorke, B. Aradi, and T. Frauenheim, Optimized hybrid functionals for defect calculations in semiconductors, J. Appl. Phys. **126**, 130901 (2019).